ORIGINAL PAPER

The influence of particle background on galaxy cluster observations of the EP-FXT

Peng Zhu[1,2] · Heng Yu[3] · Shumei Jia[1] · Chengkui Li[1] · Yong Chen[1]

Abstract

Purpose Many X-ray astronomical observatories are dedicated to observing cosmic phenomena such as galaxy clusters, which inevitably involves the influence of background. When observing the universe, there are mainly two types of background: the cosmic X-ray background and the particle background, known as non-X-ray background. Understanding the variation of the particle background is crucial for the observations made by the Einstein Probe (EP) satellite.
Methods In order to simulate the observation effects of EP-FXT, this paper utilized fixed-point observation data obtained from eROSITA's Performance Verification phase and Filter Wheel Closed data to construct a background model. Subsequently, based on the eROSITA background model, an EP-FXT background model was established. Due to the different orbits, the particle background of eROSITA is about seven times that of EP-FXT. Based on this, a comparison was made between the high-particle-background model and the low-particle-background model in the observation of galaxy clusters.
Results The results indicate that, without systematic errors, a high background leads to a 20% increase in the errors of the fitting parameter.
Conclusions The impact of systematic errors is more pronounced in observations with high particle backgrounds. Additionally, the low particle background demonstrates clear advantages in the fitting of temperature and metallicity parameters, with this advantage becoming more significant as the temperature and metallicity increase.

Keywords EP-FXT · Particle background · Galaxy cluster · XSPEC

Heng Yu, Shumei Jia, Chengkui Li and Yong Chen have contributed equally to this work.

✉ Yong Chen
ychen@ihep.ac.cn

Peng Zhu
zhupeng@ihep.ac.cn

Heng Yu
yuheng@bnu.edu.cn

Shumei Jia
jiasm@ihep.ac.cn

Chengkui Li
lick@ihep.ac.cn

[1] Key Laboratory for Particle Astrophysics, Institute of High Energy Physics, 19B Yuquan Road, Beijing 100049, China

[2] School of Physics, University of Chinese Academy of Sciences, Beijing 100049, China

[3] Astronomy Department, Beijing Normal University, Beijing 100875, China

Introduction

Many X-ray observatories are dedicated to observing astronomical phenomena such as galaxy clusters, which inevitably involve the influence of background. When observing the universe, there are mainly two types of background: the cosmic X-ray background (CXB) and the particle background, known as the non-X-ray background (NXB) [1, 2]. CXB is the uniform X-ray radiation observed in the X-ray band from the entire universe. This radiation originates from many discrete celestial bodies, such as active galactic nuclei, X-ray radiation from stars, and other high-energy celestial bodies. NXB refers to the background radiation produced by the interaction of charged particles (such as protons, alpha particles, and electrons) in cosmic rays with detector materials. Both backgrounds need to be accurately subtracted in X-ray observation and analysis. When observing galaxy clusters, accurately determining parameters such as temperature and metallicity is particularly important. In these observations, it is inevitable to consider the background, where the CXB spectrum varies with the specific region of the

sky being observed, while the NXB is only associated with the satellite's own orbit, materials, and instrument response. In low-orbit satellite observations, the primary factor contributing to the relatively lower particle background is the Earth's magnetic field, which effectively shields cosmic rays and other high-energy particles [3]. The Earth's magnetic field can efficiently mitigate the effects of cosmic rays and other high-energy particles near low-orbit satellites, reducing particle background levels. On the other hand, satellites in high orbit or those operating in deeper space may experience elevated levels of particle background due to their greater distance from the Earth's magnetic field. Consequently, they are more susceptible to the influence of cosmic rays and other high-energy particles. In observations of various component spectra, the particle background also has a significant impact on the observations of various component spectra.

Determining the in-orbit background of detectors employed in space instruments before launch is crucial in any X-ray mission development. On the one hand, these studies can be utilized to optimize spacecraft equipment designs and assess storage requirements, and to investigate whether the instrument can meet the scientific objectives. On the other hand, the estimated background helps scientists to comprehend the telescope's performance and to plan observation strategies for interested target sources, while it also assists the mission operation team to develop observation plans for the instrument. For each space instrument, background estimation is required due to the different detector type and operating environment for various orbits, such as Fioretti et al. [4] for ATHENA, Campana et al. [5] for LOFT/LAD, Xie and Pearce [6] for Sphinx, Xie et al. [7] and Zhang et al. [8] for Insight-HXMT, Tenzer et al. [9], Perinati et al. [10], and Weidenspointner et al. [11] for eROSITA, Zhao et al. [12] for the micropore Lobster-Eye Telescope (EP/WXT), and Zhang et al. [13] for the Follow-up X-ray Telescope (EP/FXT). It can be seen that in various X-ray satellites, particle background is an important influencing factor in observations.

The first Chinese X-ray-focusing satellite, 'Einstein Probe' (EP) [14], was launched into space in early 2024. This satellite carries two scientific payloads, the Wide-field X-ray Telescope (WXT) and the Follow-up X-ray Telescope (FXT) [15], to achieve comprehensive observations of celestial targets. The FXT, as a follow-up telescope, adopts a Wolter-I design for its focusing structure and employs the same PNCCD detector as eROSITA to enable spectroscopic [16], imaging, and timing observations [17]. The EP carries two efficient scientific payloads, namely the Wide-field X-ray Telescope (WXT, energy range 0.5–4 keV) and the Follow-up X-ray Telescope (FXT, energy range 0.3–10 keV). The primary task of WXT is to capture transient cosmic phenomena and continuously monitor variable celestial bodies, while FXT focuses on in-depth follow-up observations of specific targets discovered by WXT and other research facil-

ities. FXT adopts a Wolter-I type focusing mirror, divided into two units, A and B, with a structure similar to eROSITA that is equipped with seven focusing telescopes. The EP is a low-orbit scientific satellite with a lower particle background than eROSITA. According to simulations of the on-orbit EP-FXT particle background by Zhang et al. [13], the particle background of EP-FXT is approximately one-seventh that of eROSITA for the same area. Therefore, in this paper, we present the simulation of the differences in particle background levels under different conditions for observing galaxy cluster components.

This paper is organized as follows. Method section introduces how to establish the NXB model and CXB model through FWC data and blank sky data, as well as the method of spectral modeling. Data extraction and analysis section presents the data sources and background region selection. Models section introduces the model of sources, CXB, NXB, and systematic errors. Simulation results section presents and analyzes the simulated results. The final conclusion is drawn the Conclusion section.

Method

This paper used eROSITA's fixed-point observation data to construct the background model during the Performance Verification (PV) phase. The background model consists of two components, CXB and NXB. The NXB model was determined using the Filter Wheel Closed (FWC) data provided by eROSITA. In the FWC data, the filter wheel was in the closed position, blocking all X-ray signals collected by the focusing mirrors from passing through the filter wheel. Therefore, the energy spectrum observed on the PNCCD at this time was entirely attributed to the particle background. After determining all parameters in the NXB model, all parameters were fixed, and a constant was added to the overall NXB model before combining it with the CXB model and fitting it to the background in the blank sky regions, thus establishing the total background model. The sum of these two models was used as the observation background model, and the determined particle background in the eROSITA background was reduced to one-seventh as the background model for EP-FXT. Both models were used to simulate observations under different temperatures and metallicities of galaxy cluster components and under different exposure times and systematic errors.

We used the *fakeit* command in XPSEC to convert the simulated model into energy spectrum files. To assess the error of the output parameters, we performed 100 energy spectrum simulations for each scenario using the 'error' command at a 90% confidence level. This analysis was conducted based on the high-particle-background model of eROSITA and the low-particle-background model of EP-FXT. The

median of the 100 results represented the final output parameters to reduce the random fluctuations in the distribution of the output parameters to an acceptable level. Additionally, we performed error verification through 200,000 Monte Carlo simulations. The simulated spectrum is generated by utilizing our input spectrum model, ARF, and RMF, through the $fakeit$ command in XSPEC. The exposure time for the simulated spectrum is set, resulting in the generation of statistical Poisson fluctuations. Before fitting, the spectra were binned, similar to what is done with real spectra.

Data extraction and analysis

Data

The simulations in this paper are all based on the eROSITA pointed observation data, which were obtained from the early data release (EDR) of eROSITA. The EDR data includes Survey fields, Magellanic Clouds, Galactic fields, and Extragalactic fields. In this study, to investigate the impact of particle background in galaxy cluster observations, we extracted data from the galaxy cluster data, with A3158 being a relatively simple galaxy cluster in terms of structure and having a large background area in the image data, making it suitable for establishing a background model. Therefore, this paper is based on the analysis and simulation of the A3158 galaxy cluster data. The observations were carried out in September 2019 during the PV phase, using an energy range of 0.3–8 keV and with a pattern selection of 15. The parameter 'pattern' is a four-digit binary number, where each digit corresponds to a different split event. A value of 1 selects the event, while 0 discards it. Pattern = 15 corresponds to binary 1111, representing all single, double, triple, and quadruple split events.

Data extraction

Based on previous studies using eROSITA, the estimated r200 of the galaxy cluster, which represents the radius at which the average density of the cluster is 200 times the critical density of the universe, is approximately 23.95 arcmin [1]. In the observation of galaxy clusters, we believe that there are almost no cluster components beyond the r200 range. We therefore divide the whole data into galaxy cluster regions and background regions, choosing the region from 23 arcmin to 31 arcmin (corresponding to r200 to the outermost observational region) as the background extraction region, as shown in Fig. 1. In this region, we assume that the contribution of galaxy clusters is minimal. Spectra and corresponding response files were extracted from this region for background model fitting. For the region of galaxy clusters within 23 arcmin, we use it to extract approximate parame-
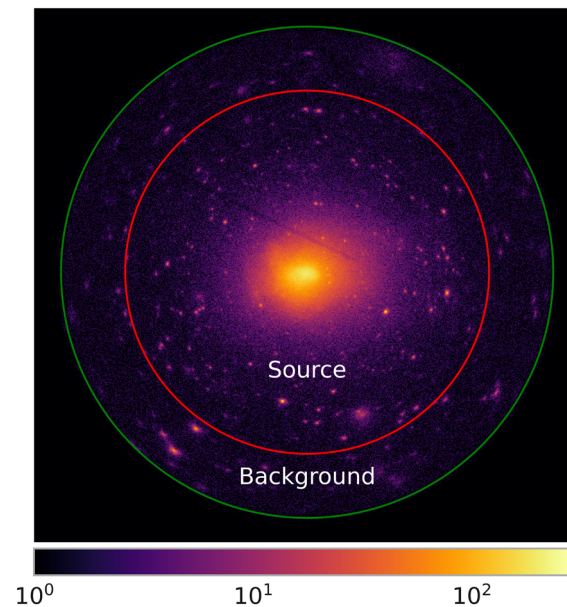

Fig. 1 The image is divided between the source region and the background region, with the source region inside the red circle and the background region between the green circle and the red circle. The red circle corresponds to the about 23 arcmin, and the green circle is the field of view boundary of about 31 arcmin

ters of the source, including temperature, metal abundance, and flux.

Models

In this paper, we constructed a combined background model consisting of particle background (NXB) and cosmic X-ray backgrounds (CXB). After excluding all point sources, we extracted spectra from a wide outer region of 23–31 arcmin and loaded them into XSPEC for analysis. The background model used in this paper consists of two parts: particle background and cosmic X-ray background.

Particle background (NXB) model

The NXB model independently describes each of the seven detectors in the early data release of eROSITA. This model combines a double power law with two additional power laws to describe continuous spectra and several instrumental lines constrained by FWC data. Parameters describing continuous medium components are fixed, with their normalization combined with the detector area. However, each detector has a separate global normalization factor for the variation of instrumental background. In the space environment, a large number of high-energy particles, such as cosmic rays and solar wind, are prevalent. These particles interact with the instrument, producing background signals that may affect

Table 1 Model parameters for the emission lines in the particle background, obtained from fitting the FWC data

Emission lines	Energy keV	Width keV	Norm
Zn-Kβ	9.57	0.0001	1.75×10^{-3}
Cu-Kβ	8.85	0.0001	2.73×10^{-18}
Zn-Kα	8.59	0.0001	6.64×10^{-3}
Ni-Kβ	8.20	0.0001	8.14×10^{-4}
Cu-Kα	8.04	0.0001	2.49×10^{-3}
Ni-Kα	7.44	0.0001	3.45×10^{-3}
Fe-Kβ	7.03	0.0001	2.32×10^{-3}
Co-Kα	6.91	0.0001	1.80×10^{-3}
Fe-Kα	6.38	0.0001	1.34×10^{-2}
Mn-Kα	5.85	0.0001	1.48×10^{-3}
Cr-Kα	5.38	0.0001	1.48×10^{-3}
Ti-Kα	4.52	0.0001	2.37×10^{-4}
Ca-Kα	3.65	0.0001	2.37×10^{-4}
Al-Kα	1.48	0.0001	1.11×10^{-2}

the accuracy and reliability of the operational data. The particle background model is established using FWC data from eROSITA, which includes continuous spectra and 14 Gaussian line spectra.

Fitting FWC data from each telescope results in the NXB model, with the analysis focusing primarily on eROSITA's telescope 1. The NXB model includes a high-energy component with an exponentially truncated power law and additional Gaussian lines, where the continuous spectral part is modeled by EXPFAC(BKN2POW+POWERLAW+ POWERLAW). The Gaussian emission lines include K_α lines of Al, Ca, Ti, Cr, Mn, Fe, Co, Ni, Cu, Zn, and K_β lines of Fe, Ni, Cu, and Zn fluorescence. This model was released by Max Planck Institute for Extraterrestrial Physics (MPE) and has been applied in the study of A3158 by Whelan et al. [1] and in the study of A3266 by Sanders et al. [18].

After loading the FWC data into XSPEC, we used the NXB background model to obtain the best-fit parameters for eROSITA, as shown in Table 1. The particle background model fits well with the actual FWC data regarding spectrum and error, as shown in Fig. 2, with a final model fit Chi-square to degrees of freedom ratio of 1.14.

Cosmic X-ray background (CXB) model

The cosmic X-ray background is a prevalent type of X-ray radiation in the universe. It is generated by high-energy events occurring in distant celestial objects, such as star formation, supernova explosions, and black hole activity. The cosmic X-ray background has significant implications for the observation and analysis of galaxy clusters. In the CXB background model, there exists a component of thermal radiation that is similar to the radiation from galaxy clusters. Therefore, precise subtraction of the CXB is crucial for studying galaxy clusters. The present model divided

Fig. 2 Particle background model. Fitting the NXB model using the FWC data of eROSITA's telescope 1
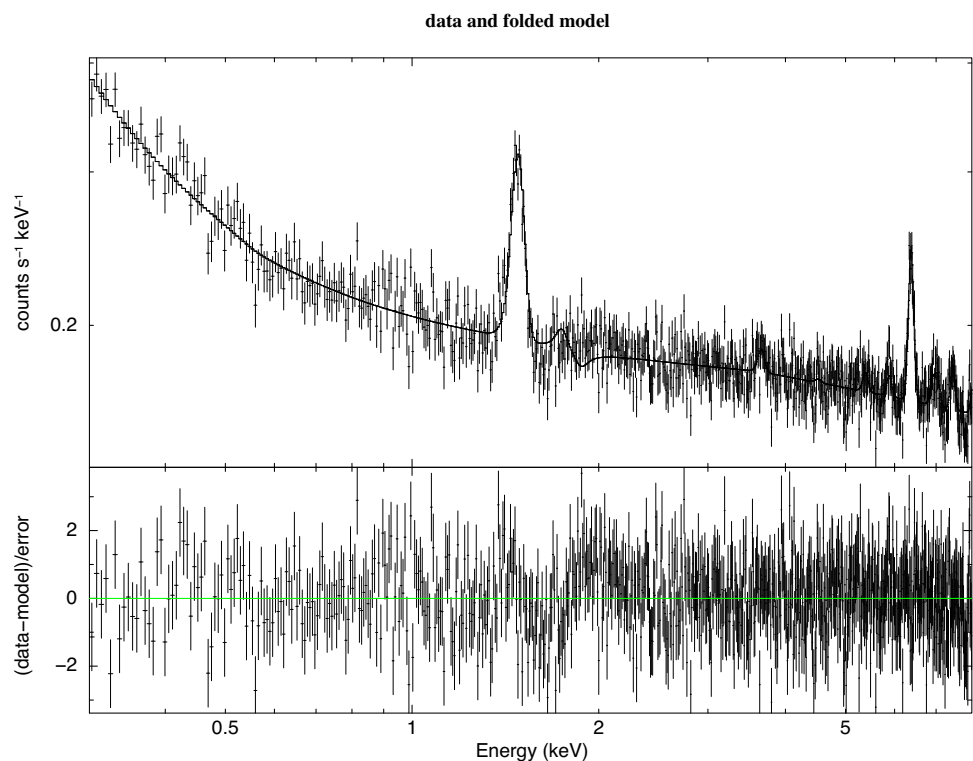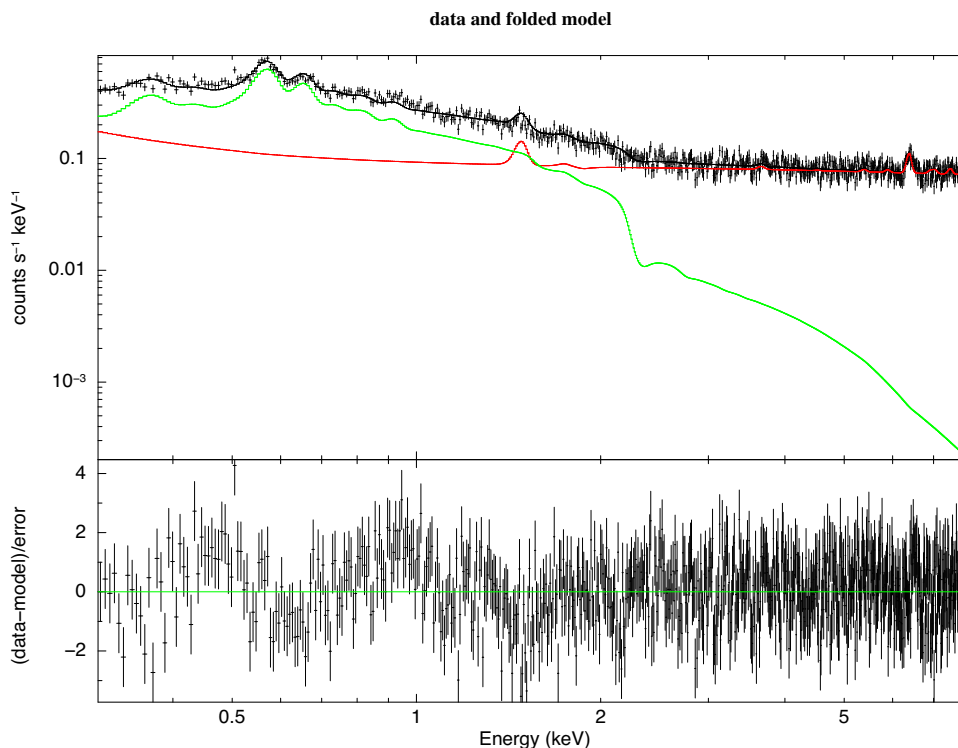

data and folded model

Fig. 3 Fitting the spectrum of the background region (23–31 arcmin) using data of eROSITA, with separate components for the NXB and CXB contributions. The solid red line represents the NXB component, while the solid green line represents the CXB component

the cosmic X-ray background into three components: an unabsorbed APEC component (at 0.099 keV) simulating the Local Hot Bubble (LHB) emission [19], an absorbed APEC component (at 0.22 keV) simulating the Milky Way Halo (MWH) emission [20], and an absorbed power-law spectrum component (with an index of 1.41) simulating an unknown component from active galactic nuclei (AGN) [21]. The absorption effects of the interstellar medium are modeled using the TBABS model [22]. The CXB model can be expressed as TBABS*(APEC+POWERLAW)+APEC. The metallicity and redshift of the two APEC components are fixed at 1.0 and 0.0, respectively.

The extracted spectra from the background region are fitted with the CXB+NXB model. Figure 3 depicts the fitted spectrum results, with a Chi-square to degrees of freedom ratio of approximately 1.26. The best-fitting parameters for the CXB are shown in Table 2.

Source model

The APEC plasma radiation model was selected as the galaxy cluster model, and the TBABS model was used to model the interstellar medium absorption. The source model is represented as TBABS*APEC. The main parameters of the source model include hydrogen column density N_H, gas temperature kT, abundance, redshift, and normalization parameter. For the selected A3158 cluster, we fixed the source redshift at 0.059 [23] and the hydrogen column density at $1.4 \times 10^{20} cm^{-2}$,

Table 2 Model parameters for the cosmic X-ray background, which is expressed by TBABS(APEC1+POWERLAW) + APEC2 using XSPEC notation

Model	Parameter	Value
TBABS	NH[1]	0.014
APEC1	kT[2]	0.22
APEC1	Abundance	1
APEC1	Redshift	0
APEC1	Norm[3]	1.2E-3
POWERLAW	Photon index	1.41
POWERLAW	Norm[4]	1.4E-3
APEC2	kT[2]	0.099
APEC2	Abundance	1
APEC2	Redshift	0
APEC2	Norm[3]	1.7E-3

[1] In units of 10^{22} cm^{-2}

[2] kT is in keV

[3] In units of $\frac{10^{-14}}{(4\pi D_A(1+z))^2} \int n_e n_H dV$, where D_A is the angular size distance to the source (cm), and n_e and n_H are the electron and H densities (cm^{-3})

[4] in units of photons/keV/cm^2 @ 1 keV

The parameters are obtained from fitting the background region after subtracting the point sources

retrieved from the Swift Scientific Data Centre, UK. In addition to fixed parameters, temperature, metallicity, and norms are determined by fitting the spectra of the cluster region. Among them, the metallicity follows the aspl standard [24],

except for the comparison of the influence of metallicity; the rest are fixed at 0.3, the temperature is selected as 5 keV, the norm value is 3.0×10^{-3}, and the corresponding flow rate is about $[0.3 - 8.0 \text{ keV}]3.8 \times 10^{-12}\text{erg/s/cm}^2$.

Systematic error

In the observation of galaxy clusters, the background is usually subtracted by using the method of subtracting the background region from the surrounding area. However, due to the effect of the focusing mirror, the CXB background is not uniformly distributed on the PNCCD detector, so correction is needed when subtracting. In contrast, the NXB background is uniformly distributed in a single observation of the PNCCD. For the observation of galaxy clusters, the observation scale is usually large, and the background area is far from the source center. Usually, a single observation cannot obtain enough data from the blank sky area, so further observations of the surrounding blank sky area are needed.

In G. Vianello's study of systematic uncertainties [25], it is discussed that the background difference between the source and background regions may be as high as 20%. The study points out that there may be systematic errors in the use of photons in the background region and analyzes the theoretical impact of systematic errors at different levels. The study concluded that a systematic error of about 10% may exist in the real observational background. On the other hand, in a study by J. F. Albacete-Colombo et al. they also used the *fakeit* command of XSPEC to simulate the data on the basis of Chandra's data and concluded that there is a systematic error of about 10% in the fitting [26]. In this

study, simulations were compared under 0%, 5%, and 10% systematic error conditions. In both models, the percentage of systematic error represents the ratio of systematic error to the total flux of the background. Compared to eROSITA, the background of EP-FXT is lower, resulting in smaller systematic errors. In this paper, a linear model was introduced to represent the systematic error of the background. Figure 4 illustrates the components of the two models and the 10% systematic error.

Simulation results

Statistical error and systematic error

First, we did not consider the impact of systematic errors and simulated a 5 keV source with a norm value of 3×10^{-3} and a metallicity of 0.3. We conducted simulations for 12 different exposure times (2 ks, 3 ks, 5 ks, 10 ks, 20 ks, 30 ks, 50 ks, 100 ks, 200 ks, 300 ks, 500 ks, and 1000 ks) to analyze the influence of particle background on the fitting results, as shown in Fig. 5. Under different exposure times, the errors for both background models showed a decreasing trend, with the high-background model resulting in significantly poorer fitting than the low-background model. Table 3 presents the results of each fitting, indicating that the error for the high background is more than 20% higher than that for the low background.

Using the same source parameters (5 keV) and exposure time selection mentioned above, we introduced a 10% systematic error to simulate the impact of the same proportion
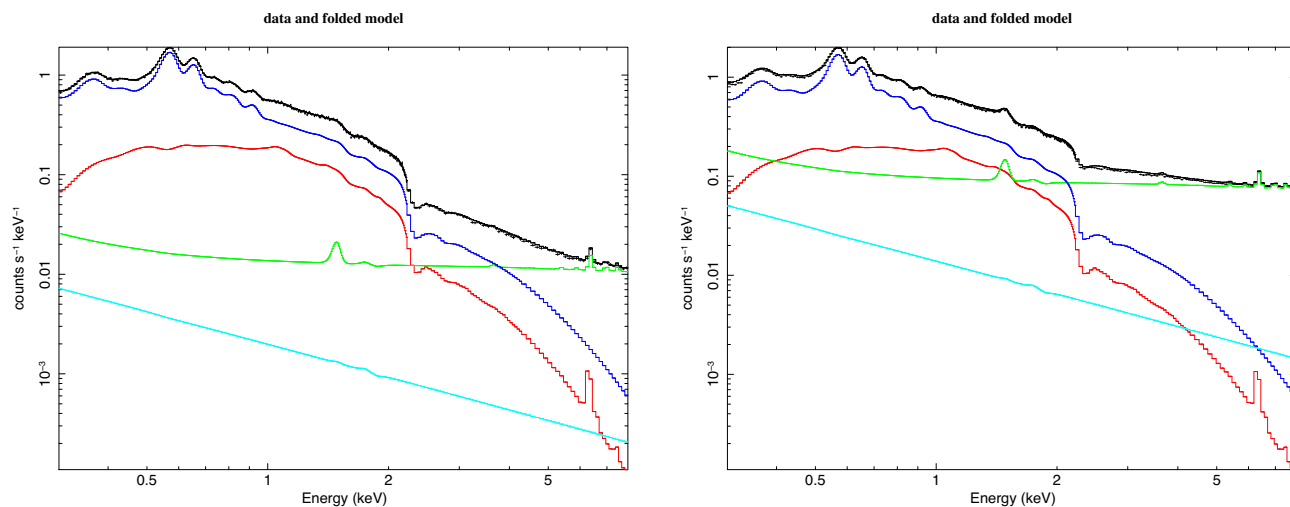

Fig. 4 The left image corresponds to the low-background model associated with EP-FXT, and the right image corresponds to the high-background model associated with eROSITA. The red line represents the galaxy cluster component, the dark blue line represents the CXB component, the green line represents the NXB component, and the light blue line represents the added systematic error, with a flux of approximately 10% of the background
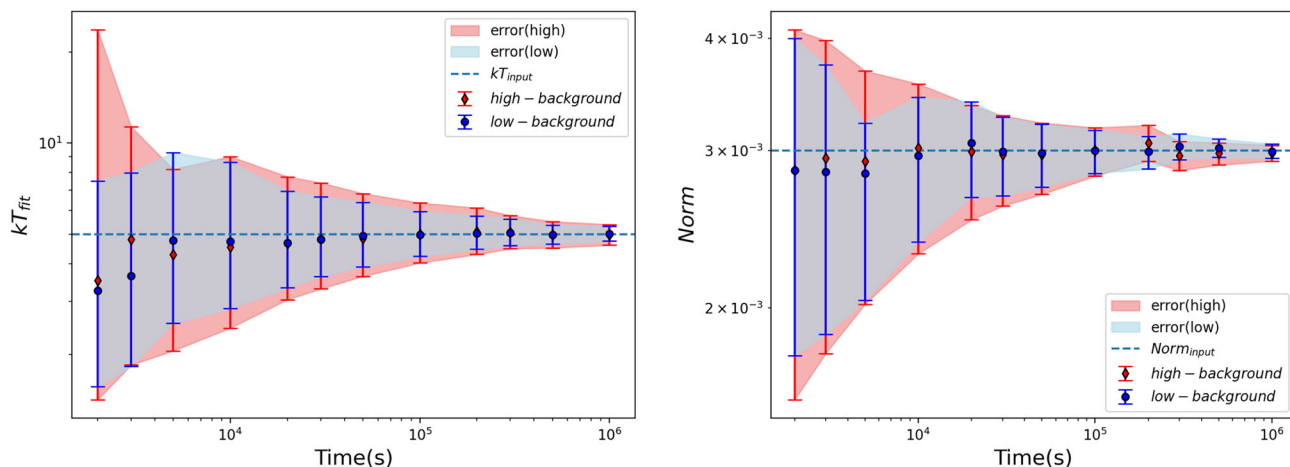
Fig. 5 Comparison of high and low backgrounds for the 5 keV galaxy cluster component under 0% system error. The EP-FXT corresponds to the low-background model, marked in blue. The eROSITA corresponds to the high-background model, marked in red. The error bars represent the range corresponding to the 90% confidence interval

Table 3 Median of 100 simulated results under different exposure times for high and low backgrounds with 0% systematic error

Exposure time ks	Low background			High background		
	kT keV	norm 10^{-3}	χ^2/dof	kT keV	norm 10^{-3}	χ^2/dof
2	$3.25^{+4.24}_{-1.68}$	$2.85^{+1.15}_{-1.08}$	1.00	$3.52^{+20.1}_{-2.10}$	$2.85^{+1.24}_{-1.27}$	1.00
3	$3.64^{+4.34}_{-1.81}$	$2.84^{+0.90}_{-0.97}$	0.99	$4.81^{+6.50}_{-2.96}$	$2.94^{+1.04}_{-1.16}$	0.99
5	$4.77^{+4.52}_{-2.23}$	$2.83^{+0.69}_{-0.79}$	1.00	$4.28^{+3.90}_{-2.22}$	$2.92^{+0.76}_{-0.90}$	1.00
10	$4.73^{+3.92}_{-1.89}$	$2.96^{+0.48}_{-0.59}$	0.98	$4.54^{+4.48}_{-2.09}$	$3.02^{+0.54}_{-0.72}$	1.06
20	$4.68^{+2.26}_{-1.35}$	$3.06^{+0.34}_{-0.40}$	1.00	$4.66^{+3.08}_{-1.62}$	$2.99^{+0.38}_{-0.48}$	1.00
30	$4.80^{+1.86}_{-1.17}$	$2.99^{+0.28}_{-0.32}$	0.99	$4.82^{+2.57}_{-1.52}$	$2.97^{+0.31}_{-0.37}$	1.00
50	$4.94^{+1.44}_{-1.03}$	$2.98^{+0.23}_{-0.25}$	0.99	$4.84^{+1.97}_{-1.21}$	$2.97^{+0.25}_{-0.29}$	1.00
100	$4.98^{+0.97}_{-0.75}$	$3.00^{+0.16}_{-0.17}$	0.98	$4.99^{+1.35}_{-0.97}$	$3.00^{+0.18}_{-0.19}$	0.99
200	$5.04^{+0.71}_{-0.57}$	$2.99^{+0.12}_{-0.13}$	1.02	$5.09^{+1.01}_{-0.80}$	$3.06^{+0.14}_{-0.14}$	0.99
300	$5.06^{+0.56}_{-0.47}$	$3.03^{+0.10}_{-0.10}$	1.00	$5.07^{+0.69}_{-0.59}$	$2.96^{+0.11}_{-0.11}$	1.00
500	$4.98^{+0.38}_{-0.33}$	$3.02^{+0.07}_{-0.07}$	1.00	$4.97^{+0.53}_{-0.46}$	$2.98^{+0.08}_{-0.09}$	1.01
1000	$5.02^{+0.29}_{-0.27}$	$2.99^{+0.06}_{-0.05}$	1.00	$4.98^{+0.40}_{-0.38}$	$2.98^{+0.06}_{-0.06}$	1.01

of systematic error between high and low backgrounds. Figure 6 presents the results, showing that the systematic error consistently leads to deviations in the final fitting results. Under 10% systematic error, the fitting results for the low-background model exhibit significantly smaller deviations. According to Table 4, at 100 ks, the fitting results tend to stabilize. The fitting result for the high background is $11.46^{+8.20}_{-3.98}$ keV, which is 2.29 times the input temperature, while the fitting result for the low background is $6.41^{+1.62}_{-1.06}$ keV, 1.28 times the input temperature, with much lower errors compared to the high-background results. Figure 7 shows that the χ^2/dof for both models increases with exposure time. At 500 ks, the high-background fitting χ^2/dof reaches 1.74, while the low background is 1.13. At 1000 ks, the high-background fitting

χ^2/dof reaches 2.65, indicating that the APEC model can no longer fit the data, while the low background χ^2/dof is only 1.19. The same proportion of systematic error has a significant impact when the particle background is high, while the EP-FXT fitting results for the low background remain within an acceptable range.

In summary, the fitting results for both backgrounds are relatively accurate without considering systematic errors and only focusing on statistical errors. The fitting error for the high background is slightly worse than that observed with the low background. However, after considering a 10% systematic error, the fitting results for the high background exhibit significant bias and larger errors, whereas the fitting results for the low background show smaller bias and errors.
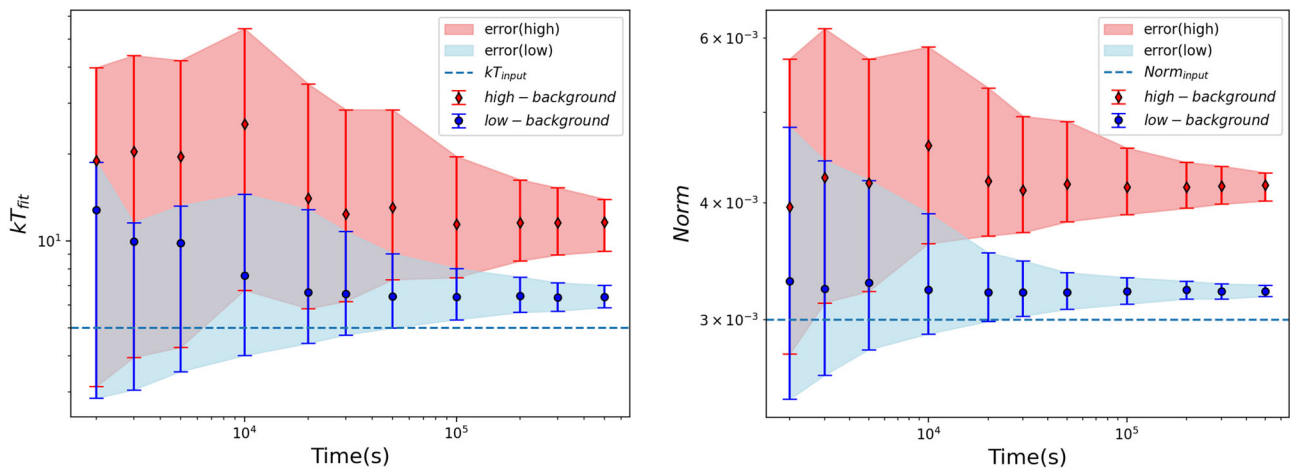
Fig. 6 Comparison of high and low backgrounds for the 5 keV galaxy cluster component under 10% system error. The EP-FXT corresponds to the low-background model, marked in blue. The eROSITA corre-sponds to the high-background model, marked in red. The error bars represent the range corresponding to the 90% confidence interval

Table 4 Median of 100 simulated results under different exposure times for high and low backgrounds with 10% systematic error

Exposure time ks	Low background			High background		
	kT keV	norm 10^{-3}	χ^2/dof	kT keV	norm 10^{-3}	χ^2/dof
2	$12.83^{+5.96}_{-9.97}$	$3.30^{+1.52}_{-0.83}$	0.98	$19.0^{+20.9}_{-15.9}$	$3.96^{+1.74}_{-1.20}$	1.01
3	$9.99^{+1.58}_{-6.93}$	$3.24^{+1.20}_{-0.62}$	0.95	$20.4^{+23.5}_{-16.5}$	$4.26^{+1.88}_{-1.13}$	0.98
5	$9.86^{+3.40}_{-6.32}$	$3.29^{+0.94}_{-0.50}$	0.99	$19.6^{+22.6}_{-15.3}$	$4.20^{+1.50}_{-0.98}$	1.01
10	$7.60^{+6.95}_{-3.58}$	$3.23^{+0.67}_{-0.33}$	0.99	$25.4^{+29.0}_{-18.6}$	$4.61^{+1.26}_{-0.99}$	1.00
20	$6.65^{+6.21}_{-2.22}$	$3.21^{+0.33}_{-0.22}$	1.00	$14.1^{+20.9}_{-8.3}$	$4.22^{+1.09}_{-0.53}$	1.02
30	$6.57^{+4.24}_{-1.83}$	$3.21^{+0.26}_{-0.18}$	0.99	$12.4^{+16.0}_{-6.2}$	$4.13^{+0.82}_{-0.41}$	1.05
50	$6.45^{+2.60}_{-1.44}$	$3.21^{+0.16}_{-0.13}$	0.99	$13.1^{+15.4}_{-5.7}$	$4.19^{+0.70}_{-0.37}$	1.08
100	$6.41^{+1.62}_{-1.06}$	$3.22^{+0.11}_{-0.10}$	1.00	$11.5^{+8.2}_{-4.0}$	$4.16^{+0.42}_{-0.27}$	1.15
200	$6.46^{+1.05}_{-0.79}$	$3.23^{+0.07}_{-0.07}$	1.02	$11.6^{+4.7}_{-3.0}$	$4.16^{+0.26}_{-0.21}$	1.32
300	$6.38^{+0.80}_{-0.65}$	$3.22^{+0.06}_{-0.06}$	1.05	$11.6^{+3.7}_{-2.6}$	$4.17^{+0.21}_{-0.18}$	1.46
500	$6.41^{+0.62}_{-0.51}$	$3.22^{+0.05}_{-0.04}$	1.13	$11.6^{+2.4}_{-2.4}$	$4.18^{+0.13}_{-0.16}$	1.74
1000	$6.34^{+0.41}_{-0.36}$	$3.22^{+0.03}_{-0.03}$	1.19			2.65

This conclusion suggests that the low-background EP-FXT model is slightly superior to eROSITA when considering only statistical errors. Furthermore, after considering the same proportion of systematic errors, the advantage of the low background becomes more pronounced.

The temperature and metallicity of galaxy clusters

As shown in Fig. 8, we conducted a detailed 3 × 3 mesh simulation for three different levels of systematic error (0%, 5%, and 10%) and exposure times (10 ks, 50 ks, and 100 ks) for five different temperatures (1.5 keV, 3 keV, 5 keV, 7 keV,

and 9 keV) of galaxy cluster components. The specific data are summarized in Tables 5 and 6.

The simulation results presented in Fig. 8 indicate the presence of statistical fluctuations in the 10 ks simulation. With an increase in exposure time, the difference between the two background models becomes more pronounced. At the 100 ks observation, the statistical error is notably small. As the simulated source temperature increases, the fitting advantage of the low-background model becomes more evident. For a 9 keV source with 0% systematic error, the fitting results for the low-background model is $8.53^{+3.17}_{-1.83}$ keV, while for the high-background model, they are $8.64^{+5.73}_{-2.28}$ keV, with errors
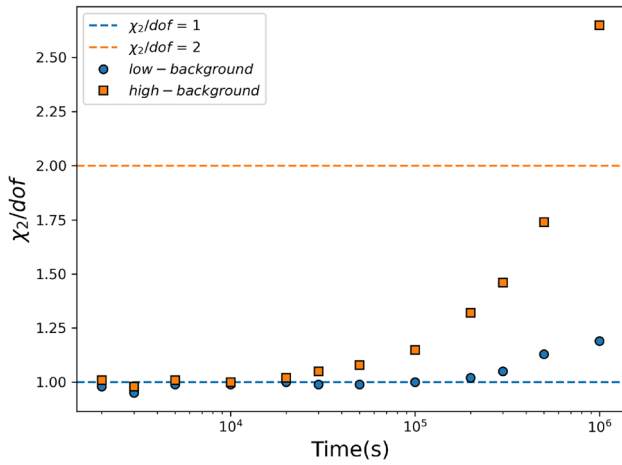
Fig. 7 Change of χ^2/dof with exposure time for high background and low background. The blue dots represent the results of the low-background model, while the orange squares correspond to the high-background model. The blue dashed line corresponds to a χ^2/dof of 1, and the orange dashed line corresponds to a χ^2/dof of 2

approximately 60% higher than those of the low-background model. With a 10% systematic error for a 9 keV source, the fitting results are $14.86^{+8.05}_{-4.37}$ keV for the low-background model and $36.05^{+36.1}_{-16.2}$ keV for the high-background model. This conclusion is mainly attributed to the dominance of the CXB in the overall background below 2 keV, resulting in a relatively small advantage for the low-background model when observing low-temperature sources. Furthermore, as the systematic error increases, the high-background model exhibits a greater overall bias and larger errors, which is consistent with the trend depicted in Fig. 6.

Metallicity is also a crucial parameter in analyzing galaxy cluster components. To investigate the influence of low particle background on the observation of sources with different metallicity values in depth, we selected five different metallicity values (0.1, 0.3, 0.5, 0.7, 0.9) of galaxy cluster components as the objects of simulation. The specific data are summarized in Tables 7 and 8.
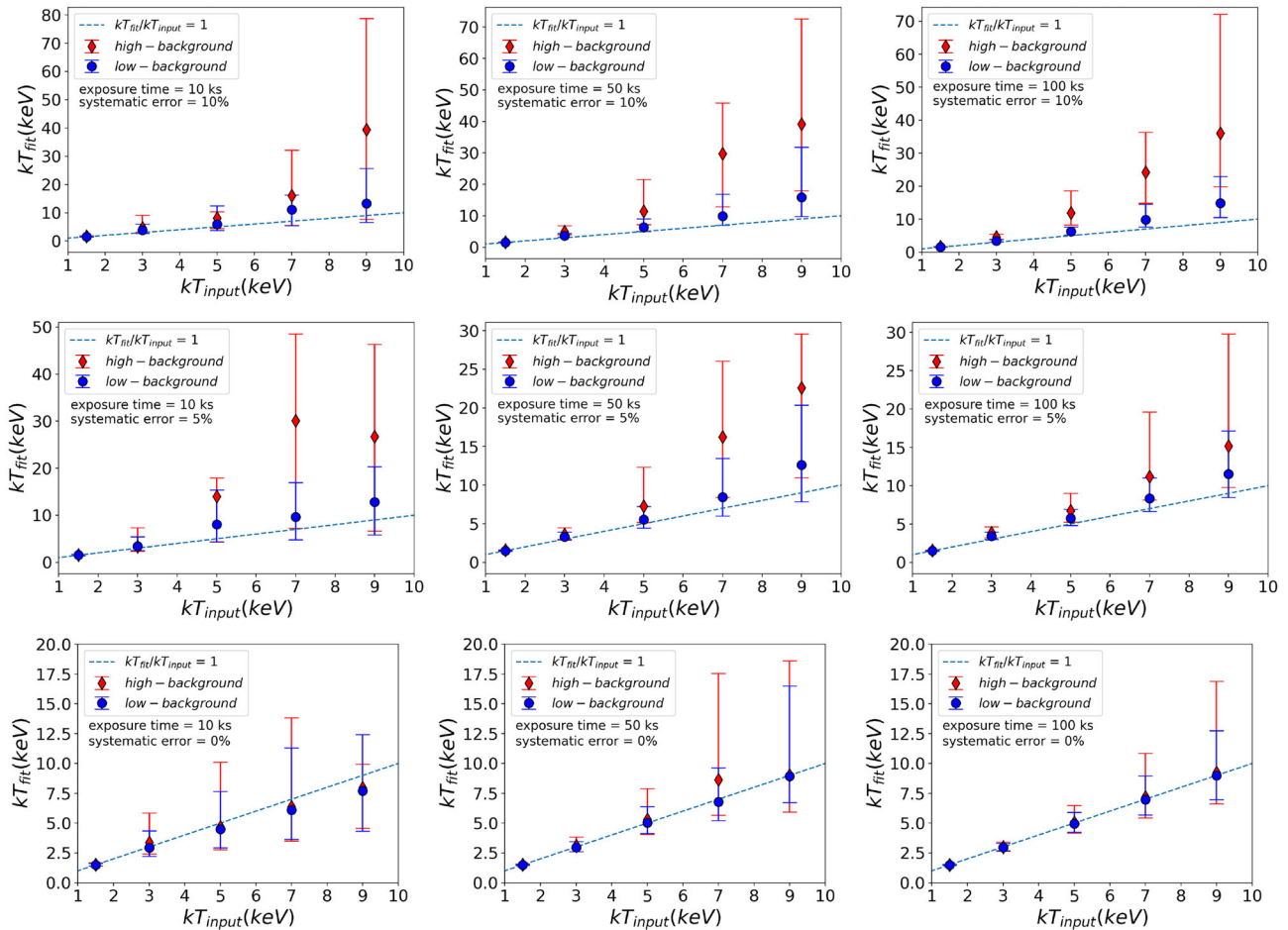

Fig. 8 The simulated results for the galaxy cluster components at five different temperatures were compared under varying system errors and exposure times. From left to right, the three columns correspond to three exposure times (10 ks, 50 ks, and 100 ks), and from bottom to top, each row corresponds to three levels of system error (0%, 5%, and 10%). The

simulated data for the low-background model corresponding to EP-FXT is marked in blue, while the simulated data for the high-background model corresponding to eROSITA is marked in red. The blue dashed line represents a ratio of 1 between the output and input parameters

Table 5 Median temperature of 100 simulated results for low background under different exposure times (10ks, 50ks, and 100ks) and different systematic errors (0%, 5%, and 10%)

kT input (keV)	Exposure time (ks)		
	10	50	100
0% systematic error			
1.50	$1.50^{+0.12}_{-0.10}$	$1.50^{+0.05}_{-0.05}$	$1.50^{+0.03}_{-0.03}$
3.00	$2.94^{+1.42}_{-0.71}$	$2.90^{+0.47}_{-0.35}$	$2.97^{+0.35}_{-0.28}$
5.00	$4.50^{+3.15}_{-1.55}$	$5.08^{+1.37}_{-0.92}$	$4.87^{+0.91}_{-0.68}$
7.00	$6.09^{+5.20}_{-2.44}$	$6.51^{+2.39}_{-1.44}$	$6.91^{+1.85}_{-1.23}$
9.00	$7.70^{+4.71}_{-3.38}$	$8.85^{+5.42}_{-2.36}$	$8.53^{+3.17}_{-1.83}$
5% systematic error			
1.50	$1.54^{+0.14}_{-0.11}$	$1.53^{+0.05}_{-0.05}$	$1.53^{+0.05}_{-0.04}$
3.00	$3.47^{+2.00}_{-0.84}$	$3.32^{+0.63}_{-0.43}$	$3.41^{+0.55}_{-0.43}$
5.00	$8.10^{+7.16}_{-3.78}$	$5.53^{+1.52}_{-1.06}$	$5.69^{+1.18}_{-0.93}$
7.00	$9.79^{+7.05}_{-4.95}$	$8.37^{+5.05}_{-2.32}$	$8.41^{+2.48}_{-1.68}$
9.00	$12.73^{+7.59}_{-6.94}$	$12.58^{+7.48}_{-4.74}$	$10.90^{+5.26}_{-2.66}$
10% systematic error			
1.50	$1.55^{+0.13}_{-0.10}$	$1.52^{+0.06}_{-0.05}$	$1.53^{+0.04}_{-0.03}$
3.00	$3.82^{+2.20}_{-1.15}$	$3.51^{+0.68}_{-0.50}$	$3.42^{+0.44}_{-0.35}$
5.00	$5.87^{+6.64}_{-2.09}$	$6.04^{+2.28}_{-1.24}$	$6.23^{+1.39}_{-1.00}$
7.00	$11.06^{+5.23}_{-5.55}$	$8.65^{+6.01}_{-2.27}$	$9.85^{+4.76}_{-2.21}$
9.00	$13.30^{+12.4}_{-6.70}$	$14.59^{+14.3}_{-5.33}$	$14.86^{+8.05}_{-4.37}$

Table 6 Median temperature of 100 simulated results for high background under different exposure times (10 ks, 50 ks, and 100 ks) and different systematic errors (0%, 5%, and 10%)

kT input (keV)	Exposure time (ks)		
	10	50	100
0% systematic error			
1.50	$1.53^{+0.15}_{-0.11}$	$1.51^{+0.06}_{-0.05}$	$1.50^{+0.04}_{-0.04}$
3.00	$3.38^{+2.48}_{-0.98}$	$3.07^{+0.69}_{-0.46}$	$2.96^{+0.43}_{-0.33}$
5.00	$4.69^{+5.43}_{-1.92}$	$4.87^{+1.77}_{-1.06}$	$5.01^{+1.34}_{-0.88}$
7.00	$6.36^{+7.49}_{-2.85}$	$6.79^{+4.34}_{-1.90}$	$6.93^{+2.88}_{-1.57}$
9.00	$7.94^{+2.00}_{-3.36}$	$8.59^{+8.29}_{-2.91}$	$8.64^{+5.73}_{-2.28}$
5% systematic error			
1.50	$1.68^{+0.05}_{-0.05}$	$1.53^{+0.06}_{-0.06}$	$1.55^{+0.05}_{-0.05}$
3.00	$3.47^{+3.90}_{-1.05}$	$3.63^{+0.84}_{-0.63}$	$3.79^{+0.80}_{-0.64}$
5.00	$13.79^{+4.11}_{-9.26}$	$7.21^{+5.05}_{-2.00}$	$6.63^{+1.99}_{-1.43}$
7.00	$29.90^{+18.3}_{-22.4}$	$16.26^{+9.69}_{-7.89}$	$11.43^{+8.12}_{-3.15}$
9.00	$26.53^{+19.5}_{-19.8}$	$22.58^{+6.94}_{-11.6}$	$15.52^{+13.2}_{-5.45}$
10% systematic error			
1.50	$1.65^{+0.18}_{-0.13}$	$1.66^{+0.07}_{-0.07}$	$1.65^{+0.05}_{-0.05}$
3.00	$4.65^{+4.53}_{-1.54}$	$4.71^{+1.57}_{-0.92}$	$4.55^{+0.91}_{-0.64}$
5.00	$8.12^{+.24}_{-3.72}$	$9.13^{+9.90}_{-2.85}$	$11.85^{+6.78}_{-3.55}$
7.00	$16.05^{+16.1}_{-10.5}$	$25.00^{+23.9}_{-11.8}$	$24.26^{+12.1}_{-9.44}$
9.00	$39.36^{+39.1}_{-31.8}$	$33.35^{+33.4}_{-18.4}$	$36.05^{+36.1}_{-16.2}$

Through simulation analysis, we obtained the results of different metallicity under different exposure times (10 ks, 50 ks, and 100 ks) and systematic errors (10%, 5%, and 0%), as shown in Fig. 9. When observing galaxy cluster components with high metallicity, for example, at 0.7 metallicity and 100 ks exposure with 0% systematic error, the fitting results for the low-background and high-background models are $0.67^{+0.35}_{-0.23}$ and $0.74^{+0.54}_{-0.29}$, respectively, as depicted in Fig. 9. The error interval of the low-background model fitting results is approximately 70% of that of the high-background model. As the systematic error increases, the fitting parameters obtained from high particle background deviate further, and the errors become larger. In the fitting results for a metallicity of 0.7, the low-background model deviates by 0.03, 0.1, and 0.36 in different systematic errors, while the high-background model deviates by 0.04, 0.21, and 0.63. These findings indicate that particle background also has a certain impact on the accuracy of fitting metallicity. Hence, a high particle background leads to large statistical and systematic errors, affecting the true metallicity.

To verify the fitting of the correlation between temperature distribution and metallicity, we conducted MCMC simulations for the two background models in three different exposure times, we obtained comprehensive probability distribution plots for the fitting results of temperature and metallicity. The figure provides a detailed display of the comprehensive probability distribution of temperature and metallicity obtained through MCMC simulation at three different exposure times: 10 ks, 50 ks, and 100 ks. The red, green, and blue lines indicate the 1σ, 2σ, and 3σ error ranges, respectively.

Figure 10 shows that the error range is particularly evident under the 10 ks observation condition, and the overall fitting accuracy is relatively low. However, the low-background model has smaller errors. As the observation time increases, the errors in the fitting of temperature and metallicity for the low-background model gradually decrease, while the errors for the high-background model remain relatively large. This conclusion validates the significant difference in errors between the high- and low-background models, as shown in Figs. 8 and 9.

Table 7 Median abundance of 100 simulated results for low background under different exposure times (10 ks, 50 ks, and 100 ks) and different systematic errors (0%, 5%, and 10%)

Abundance input	Exposure time (ks)		
	10	50	100
0% systematic error			
0.10	$0.06^{+0.93}_{-0.06}$	$0.07^{+0.33}_{-0.07}$	$0.13^{+0.20}_{-0.12}$
0.30	$0.26^{+0.97}_{-0.24}$	$0.22^{+0.38}_{-0.21}$	$0.28^{+0.24}_{-0.17}$
0.50	$0.55^{+1.37}_{-0.44}$	$0.39^{+0.39}_{-0.23}$	$0.43^{+0.27}_{-0.18}$
0.70	$0.54^{+1.29}_{-0.43}$	$0.63^{+0.56}_{-0.30}$	$0.67^{+0.35}_{-0.23}$
0.90	$0.80^{+1.56}_{-0.60}$	$0.90^{+0.54}_{-0.35}$	$0.97^{+0.43}_{-0.30}$
5% systematic error			
0.10	$0.06^{+1.39}_{-0.06}$	$0.15^{+0.48}_{-0.13}$	$0.10^{+0.24}_{-0.10}$
0.30	$0.17^{+1.06}_{-0.17}$	$0.46^{+0.57}_{-0.31}$	$0.34^{+0.31}_{-0.21}$
0.50	$0.45^{+1.50}_{-0.43}$	$0.64^{+0.69}_{-0.38}$	$0.63^{+0.41}_{-0.27}$
0.70	$0.63^{+1.73}_{-0.57}$	$0.75^{+0.63}_{-0.37}$	$0.80^{+0.43}_{-0.29}$
0.90	$0.94^{+1.94}_{-0.74}$	$1.12^{+0.86}_{-0.49}$	$1.00^{+0.46}_{-0.31}$
10% systematic error			
0.10	$0.18^{+0.48}_{-0.18}$	$0.16^{+0.63}_{-0.16}$	$0.12^{+0.43}_{-0.12}$
0.30	$0.66^{+0.64}_{-0.58}$	$0.37^{+0.63}_{-0.34}$	$0.49^{+0.50}_{-0.33}$
0.50	$0.81^{+0.74}_{-0.67}$	$0.81^{+0.81}_{-0.43}$	$0.77^{+0.53}_{-0.34}$
0.70	$0.98^{+0.72}_{-0.80}$	$1.25^{+1.02}_{-0.60}$	$1.06^{+0.56}_{-0.38}$
0.90	$1.69^{+0.62}_{-1.21}$	$1.17^{+0.89}_{-0.53}$	$1.34^{+0.60}_{-0.42}$

Table 8 Median abundance of 100 simulated results for high background under different exposure times (10 ks, 50 ks, and 100 ks) and different systematic errors (0%, 5%, and 10%)

Abundance input	Exposure time (ks)		
	10	50	100
0% systematic error			
0.10	$0.07^{+1.13}_{-0.07}$	$0.04^{+0.31}_{-0.04}$	$0.03^{+0.23}_{-0.03}$
0.30	$0.19^{+1.00}_{-0.18}$	$0.32^{+0.64}_{-0.27}$	$0.27^{+0.30}_{-0.18}$
0.50	$0.43^{+1.55}_{-0.40}$	$0.60^{+0.85}_{-0.36}$	$0.47^{+0.35}_{-0.21}$
0.70	$0.74^{+2.10}_{-0.60}$	$0.63^{+0.71}_{-0.33}$	$0.74^{+0.54}_{-0.29}$
0.90	$0.75^{+1.85}_{-0.59}$	$0.87^{+0.89}_{-0.43}$	$0.90^{+0.56}_{-0.32}$
5% systematic error			
0.10	$0.01^{+1.19}_{-0.01}$	$0.24^{+0.67}_{-0.24}$	$0.01^{+0.46}_{-0.01}$
0.30	$0.29^{+1.47}_{-0.29}$	$0.65^{+0.87}_{-0.54}$	$0.28^{+0.46}_{-0.24}$
0.50	$0.44^{+1.32}_{-0.44}$	$1.06^{+0.77}_{-0.70}$	$0.78^{+0.82}_{-0.44}$
0.70	$0.75^{+2.08}_{-0.60}$	$1.09^{+1.22}_{-0.64}$	$0.91^{+0.81}_{-0.45}$
0.90	$1.17^{+2.30}_{-0.98}$	$1.46^{+1.44}_{-0.81}$	$1.27^{+0.87}_{-0.51}$
10% systematic error			
0.10	$0.03^{+0.01}_{-0.03}$	$0.00^{+1.10}_{-0.00}$	$0.00^{+0.82}_{-0.00}$
0.30	$1.12^{+0.39}_{-1.01}$	$0.31^{+1.43}_{-0.31}$	$0.28^{+0.92}_{-0.28}$
0.50	$1.34^{+0.97}_{-1.23}$	$0.85^{+1.69}_{-0.65}$	$0.84^{+1.03}_{-0.60}$
0.70	$1.67^{+0.88}_{-1.52}$	$1.35^{+1.32}_{-0.82}$	$1.33^{+1.31}_{-0.74}$
0.90	$1.93^{+1.30}_{-1.43}$	$2.05^{+1.21}_{-1.14}$	$1.79^{+1.32}_{-0.78}$

Conclusion

This paper compared the observational performance of the low-particle-background model corresponding to EP-FXT and the high-particle-background model under different exposure times and levels of systematic error. In the simulation process, a linear systematic error was introduced, and simulations were conducted for different exposure times and various temperature and metallicity levels of galaxy clusters under different systematic errors. The conclusions drawn from the simulation results are as follows:

- Under different exposure times, with 0% systematic error in the correct results, the error of the high-background model is about 20% higher than that of the low-background model, and there is no systematic bias in the fitting results. When the systematic error is 10%, the high-background model deviates by 149%, while the low-background model deviates by 28%. As the observation time increases, the fitting quality gradually deteriorates. At 1 Ms, the χ^2/dof for the high-background model is 2.65, indicating an inability to fit the components of the galaxy cluster. It can be seen that the low-background

model provides more accurate parameter fitting, with less susceptibility to systematic errors.

- In the fitting results for galaxy clusters at five different temperatures, the advantage of the low-background model becomes more pronounced as the temperature increases. Without considering systematic errors, at 9 keV, the high-background model has 60% higher error than the low-background model, a significant increase from the 20% difference at 5 keV. Furthermore, as the systematic error increases, the deviation of the fitting values gradually increases, with this trend being more pronounced in the high-background model.
- In the fitting results for galaxy clusters at five different metallicity levels, a similar trend to the temperature is observed. At a metallicity of 0.9, the high-background model's error is 43% higher than that of the low-background model, while at 0.3, the high-background model's error is 17% higher. With increasing metallicity, the error introduced by the high-background model slightly increases. The change in trend with increasing systematic error is similar to that of the temperature parameter.
- In the comprehensive probability plot of the MCMC simulation results, it is evident that the error in the compre-
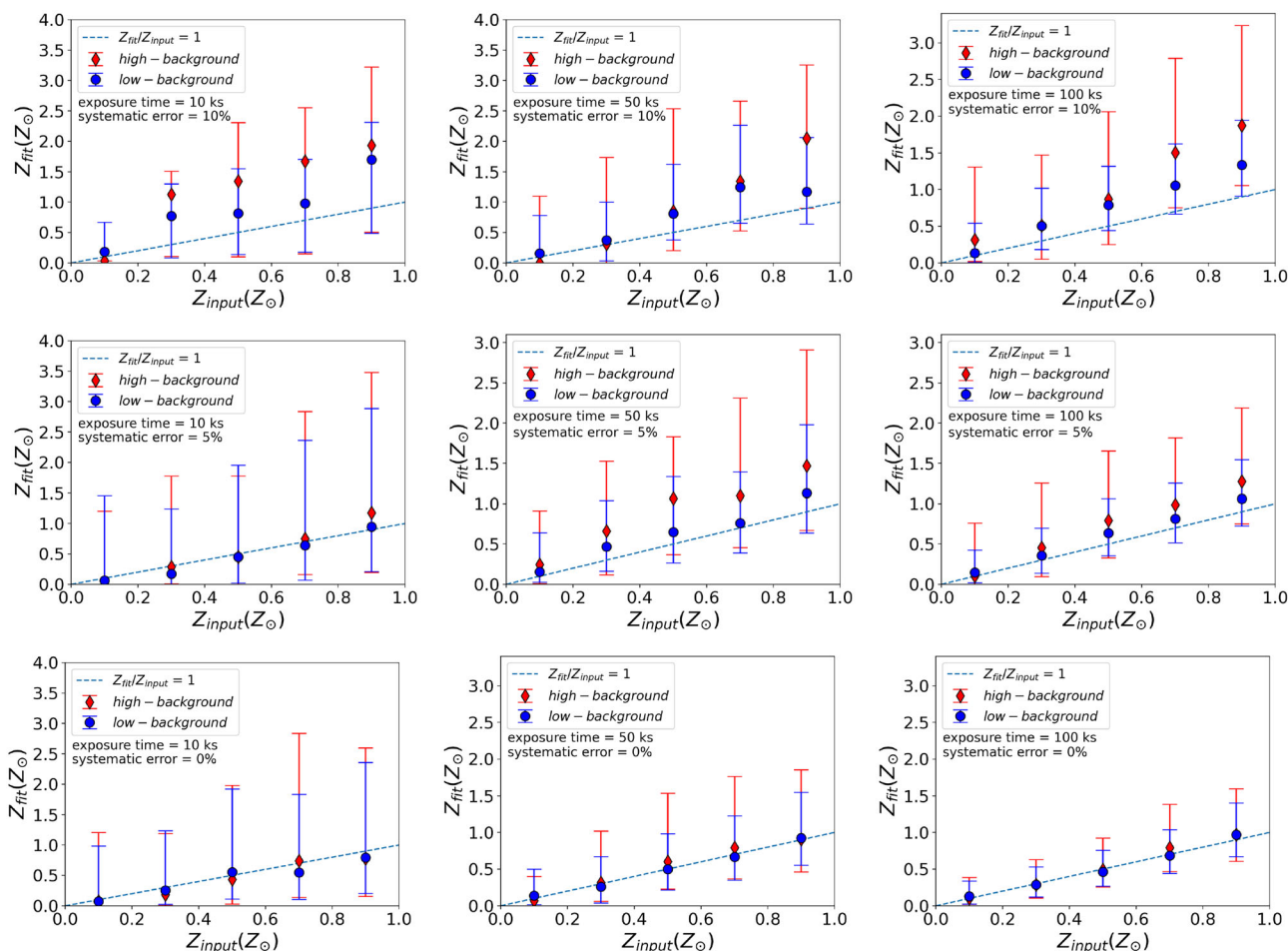
Fig. 9 The simulated results for the galaxy cluster components at five different metallicities were compared under varying system errors and exposure times. From left to right, the three columns correspond to three exposure times (10 ks, 50 ks, and 100 ks), and from bottom to top, each row corresponds to three levels of system error (0%, 5%, and 10%). The simulated data for the low-background model corresponding to EP-FXT is marked in blue, while the simulated data for the high-background model corresponding to eROSITA is marked in red. The blue dashed line represents a ratio of 1 between the output and input parameters

hensive probability distribution of the high-background model is higher than that of the low-background model for both parameters, with the error in metallicity being particularly large, indicating greater uncertainty in the fitting process.

In conclusion, the EP-FXT demonstrates a clear advantage in observing high-temperature components of galaxy clusters, and exhibits a certain advantage in fitting metallicity compared to the high-background model. Furthermore, the impact of systematic error caused by the low background is relatively small, which provides valuable reference for future observations of galaxy clusters using EP-FXT.
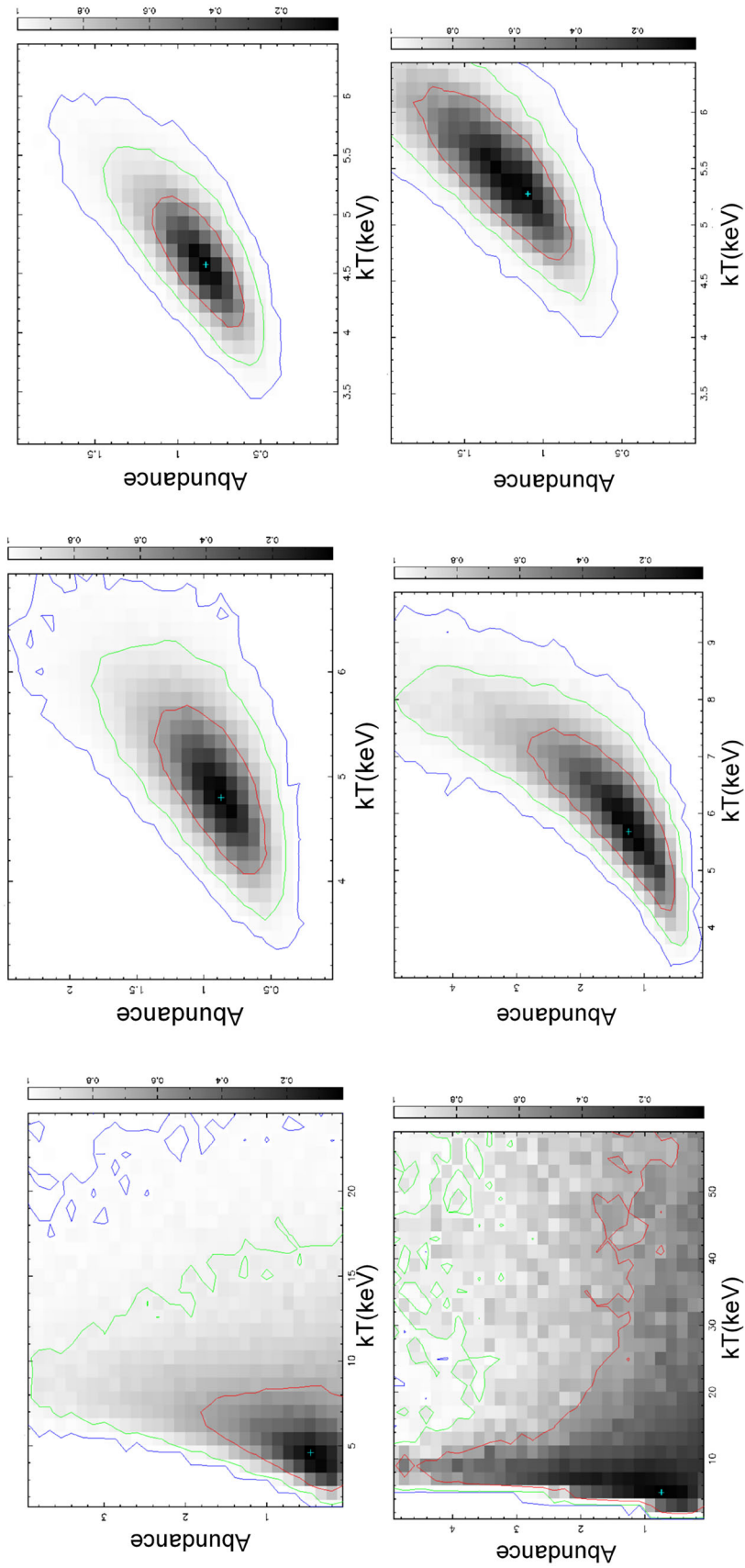
Fig. 10 Comprehensive probability plots for MCMC simulation (200,000 steps). The comprehensive probability distribution plots from left to right correspond to exposure times of 10 ks, 50 ks, and 100 ks. The top row shows the results for the low-background model, while the bottom row displays the fitting results for the high-background model

Declarations

Conflict of interest On behalf of all authors, the corresponding author states that there is no conflict of interest.

References

1. B. Whelan, A. Veronica, F. Pacaud, T.H. Reiprich, E. Bulbul, M.E. Ramos-Ceja, J.S. Sanders, J. Aschersleben, J. Iljenkarevic, K. Migkas, M. Freyberg, K. Dennerl, M. Kara, A. Liu, V. Ghirardini, N. Ota, X-ray studies of the abell 3158 galaxy cluster with erosita. Astron. Astrophys. **663**, 171 (2022). https://doi.org/10.1051/0004-6361/202141621
2. I. Bartalucci, P. Mazzotta, H. Bourdin, A. Vikhlinin, Chandraacis-i particle background: an analytical model. Astron. Astrophys. **566**, 25 (2014). https://doi.org/10.1051/0004-6361/201423443
3. C.E. Grant, E.D. Miller, M.W. Bautz, R. Foster, R.P. Kraft, S. Allen, D.N. Burrows, Towards precision particle background estimation for future X-ray missions: correlated variability between Chandra ACIS and AMS (2022)
4. V. Fioretti, A. Bulgarelli, G. Malaguti, D. Spiga, A. Tiengo, *Monte carlo simulations of soft proton flares: testing the physics with xmm-newton*, in *Astronomical Telescopes + Instrumentation* (2016). https://api.semanticscholar.org/CorpusID:119021491
5. R. Campana, M. Feroci, E. Del Monte, T. Mineo, N. Lund, G.W. Fraser, Background simulations for the large area detector onboard loft. Exp. Astron. **36**(3), 451–477 (2013). https://doi.org/10.1007/s10686-013-9341-6
6. F. Xie, M. Pearce, A study of background conditions for sphinx–the satellite-borne gamma-ray burst polarimeter. Galaxies **6**(2), 50 (2018). https://doi.org/10.3390/galaxies6020050
7. F. Xie, J. Zhang, L.-M. Song, S.-L. Xiong, J. Guan, Simulation of the in-flight background for HXMT/HE. **360**, 13 (2015). https://doi.org/10.1007/s10509-015-2559-1. arXiv:1511.02997 [astro-ph.IM]
8. J. Zhang, X. Li, M. Ge, H. Zhao, Y. Tuo, F. Xie, G. Li, S. Zheng, J. Nie, L. Song, A. Zhang, Y. Yang, Y. Chen, Comparison of simulated backgrounds with in-orbit observations for he, me, and le onboard insight-hxmt. Astrophys. Space Sci. (2020). https://doi.org/10.1007/s10509-020-03873-8
9. C. Tenzer, G. Warth, E. Kendziorra, A. Santangelo, *Geant4 simulation studies of the erosita detector background*, in *Astronomical Telescopes + Instrumentation* (2010). https://api.semanticscholar.org/CorpusID:122309027
10. E. Perinati, C. Tenzer, A. Santangelo, K. Dennerl, M.J. Freyberg, P. Predehl, The radiation environment in l-2 orbit: implications on the non-x-ray background of the erosita pn-ccd cameras. Exp. Astron. **33**, 39–53 (2012)
11. G. Weidenspointner, M.G. Pia, A. Zoglauer, *Application of the geant4 pixe implementation for space missions new models for pixe simulation with geant4*, in *2008 IEEE Nuclear Science Symposium Conference Record* (2008), pp. 2877–2884
12. D. Zhao, C. Zhang, W. Yuan, S.-N. Zhang, R. Willingale, Z. Ling, Geant4 simulations of a wide-angle x-ray focusing telescope. Exp. Astron. **43**, 267–283 (2017)
13. J. Zhang, L. Qi, Y. Yang, J. Wang, Y. Liu, W. Cui, D. Zhao, S. Jia, T. Li, T. Chen, G. Li, X. Zhao, Y. Chen, H. Liu, C. Bao, J. Guan, L. Song, W. Yuan, Estimate of the background and sensitivity of the follow-up x-ray telescope onboard Einstein probe. Astropart.

14. Phys. **137**, 102668 (2022). https://doi.org/10.1016/j.astropartphys.2021.102668
14. W. Yuan, C. Zhang, Y. Chen, Z. Ling, *The Einstein Probe Mission*, in *Handbook of X-ray and Gamma-ray Astrophysics* (2022), p. 86. https://doi.org/10.1007/978-981-16-4544-0_151-1
15. Y. Chen, W. Cui, D. Han, J. Wang, Y. Yang, Y. Wang, W. Li, J. Ma, Y. Xu, F. Lu, H. Chen, Q. Tang, W. Yuan, P. Friedrich, N. Meidinger, I. Keil, V. Burwitz, J. Eder, K. Hartmann, K. Nandra, A. Keereman, A. Santovincenzo, D. Vernani, G. Bianucci, G. Valsecchi, B. Wang, L. Wang, D. Wang, D. Li, L. Sheng, P. Qiang, R. Shi, X. Chao, Z. Song, Z. Zhang, J. Huo, H. Wang, M. Cong, X. Yang, D. Hou, X. Zhao, Z. Zhao, T. Chen, M. Li, T. Zhang, L. Luo, J. Xu, G. Li, Q. Zhang, X. Bi, Y. Zhu, N. Yu, C. Chen, Z. Lv, B. Lu, J. Zhang, *Status of the follow-up x-ray telescope onboard the Einstein probe satellite*, in Herder, J.-W.A., Nikzad, S., Nakazawa, K. (eds.) *Space Telescopes and Instrumentation 2020: Ultraviolet to Gamma Ray*, vol. 11444. SPIE (2020), p. 114445. https://doi.org/10.1117/12.2562311
16. N. Meidinger, R. Andritschke, S. Ebermayer, J. Elbs, O. Hälker, R. Hartmann, S.C. Herrmann, N. Kimmel, G. Schächner, F. Schopper, H. Soltau, L. Strüder, G. Weidenspointner, Development of the focal plane pnccd camera system for the x-ray space telescope Erosita. Nucl. Instrum. Methods Phys. Res. Sect. A Accelerat. Spectrom. Detect. Associa. Equipm. **624**, 321–329 (2010)
17. W. Yuan, C. Zhang, Y. Chen, S. Sun, Y. Zhang, W. Cui, Z. Ling, M. Huang, D. Zhao, W. Wang, Y. Qiu, Z. Liu, H. Pan, H. Cai, J. Deng, Z. Jia, C. Jin, H. Sun, H. Hu, F. Liu, M. Zhang, L. Song, F. Lu, S. Jia, C. Li, H. Zhao, M. Ge, J. Zhang, W. Cui, Y. Wang, J. Wang, X. Sun, G. Jin, L. Li, F. Chen, Z. Cai, T. Guo, G. Liu, H. Liu, H. Feng, S. Zhang, B. Zhang, Z. Dai, X. Wu, L. Gou, Einstein Probe: exploring the ever-changing X-ray Universe. Sci. Sin. Phys. Mech. Astronom. **48**(3), 039502 (2018). https://doi.org/10.1360/SSPMA2017-00297
18. J.S. Sanders, V. Biffi, M. Brüggen, E. Bulbul, K. Dennerl, K. Dolag, T. Erben, M. Freyberg, E. Gatuzz, V. Ghirardini, D.N. Hoang, M. Klein, A. Liu, A. Merloni, F. Pacaud, M.E. Ramos-Ceja, T.H. Reiprich, J.A. ZuHone, Studying the merging cluster Abell 3266 with Erosita. Astron. Astrophys. **661**, 36 (2022). https://doi.org/10.1051/0004-6361/202141501
19. R.K. Smith, N.S. Brickhouse, D.A. Liedahl, J.C. Raymond, Collisional plasma models with apec/aped: emission-line diagnostics of hydrogen-like and helium-like ions. Astrophys. J. **556**(2), 91–95 (2001). https://doi.org/10.1086/322992
20. D. McCammon, R. Almy, E. Apodaca, W. Bergmann Tiest, W. Cui, S. Deiker, M. Galeazzi, M. Juda, A. Lesser, T. Mihara, J.P. Morgenthaler, W.T. Sanders, J. Zhang, E. Figueroa-Feliciano, R.L. Kelley, S.H. Moseley, R.F. Mushotzky, F.S. Porter, C.K. Stahle, A.E. Szymkowiak, A high spectral resolution observation of the soft X-ray diffuse background with thermal detectors. **576**(1), 188–203 (2002). https://doi.org/10.1086/341727. arXiv:astro-ph/0205012 [astro-ph]
21. A. De Luca, S. Molendi, The 2–8 keV cosmic X-ray background spectrum as observed with XMM-Newton. **419**, 837–848 (2004). https://doi.org/10.1051/0004-6361:20034421. arXiv:astro-ph/0311538 [astro-ph]
22. J. Wilms, A. Allen, R. McCray, On the absorption of X-rays in the interstellar medium. **542**(2), 914–924 (2000). https://doi.org/10.1086/317016. arXiv:astro-ph/0008425 [astro-ph]
23. M.F. Struble, H.J. Rood, A compilation of redshifts and velocity dispersions for aco clusters. Astrophys. J. Suppl. Ser. **125**(1), 35 (1999). https://doi.org/10.1086/313274
24. M. Asplund, N. Grevesse, A.J. Sauval, P. Scott, The chemical composition of the sun. Ann. Rev. Astron. Astrophys. **47**(1), 481–522 (2009). https://doi.org/10.1146/annurev.astro.46.060407.145222
25. G. Vianello, The significance of an excess in a counting experiment: assessing the impact of systematic uncertainties and the case with a

gaussian background. Astrophys. J. Suppl. Ser. **236**(1), 17 (2018). https://doi.org/10.3847/1538-4365/aab780

26. J.F. Albacete-Colombo, E. Flaccomio, J.J. Drake, N.J. Wright, M. Guarcello, V. Kashyap, The statistical uncertainties on x-ray flux and spectral parameters from chandra acis-i observations of faint sources: application to the cygnus ob2 association. Astrophys. J. Suppl. Ser. **269**(1), 11 (2023). https://doi.org/10.3847/1538-4365/acdd69